

Polarization of high-energy emissions from the Crab pulsar

J. Takata

ASIAA/National Tsing Hua University - TIARA, PO Box 23-141, Taipei, Taiwan

takata@tiara.sinica.edu.tw

H.-K. Chang

*Department of Physics and Institute of Astronomy, National Tsing Hua University,
Hsinchu 30013, Taiwan*

and

K.S. Cheng

Department of Physics, University of Hong Kong, Pokfulam Road, Hong Kong, China

ABSTRACT

We investigate polarization of high-energy emissions from the Crab pulsar in the frame work of the outer gap accelerator, following previous works of Cheng and coworkers. The recent version of the outer gap, which extends from inside the null charge surface to the light cylinder, is used for examining the synchrotron radiations from the secondary and the tertiary pairs, which are produced outside the gap. We calculate the light curve, the spectrum and the polarization characteristics, simultaneously, by taking into account gyration motion of the particles. The polarization position angle curve and the polarization degree are calculated to compare with the Crab optical data. We demonstrate that the radiations from inside the null charge surface make outer-wing and off-pulse emissions in the light curve, and the tertiary pairs contribute to bridge emissions. The emissions from the secondary pairs explain the main features of the observed light curve and spectrum. On the other hand, both emissions from inside the null charge surface and from the tertiary pairs are required to explain the optical polarization behavior of the Crab pulsar. The energy dependence of the polarization features is expected by the present model. For the Crab pulsar, the polarization position angle curve indicates that the viewing angle of the observer measured from the rotational axis is greater than 90° .

Subject headings: optical:theory-polarization-pulsars:individual:PSR B0531+21-radiation mechanism:non-thermal

1. INTRODUCTION

The *Compton Gamma-Ray Observatory* (CGRO) had shown that young pulsars are strong γ -ray sources, and had detected seven γ -ray pulsars (Thompson et al. 1999). The CGRO revealed that the light curve with double peaks in a period and the spectrum extending to above GeV are typical features of the high-energy emissions from the γ -ray pulsars. Although these data have constrained proposed models, the origin of the γ -ray emission is not yet conclusive. One important reason is that various models have successfully explained the features of the observed spectra and/or light curves. For example, in the frame works of the polar cap model (Daugherty & Harding 1996), the two-pole caustic model (Dyks & Rudak 2003) and the outer gap model (Romani & Yadigaroglu 1995; Cheng et al. 2000, hereafter CRZ00), the main features of the observed light curve such as two peaks in a period and the emissions between the two peaks are all expected. So, we cannot discriminate the three different models using the observed light curve. Furthermore, both the polar cap and outer gap models have explained the observed γ -ray spectrum (Daugherty & Harding 1996; Romani 1996).

Polarization measurement will play an important role to discriminate the various models, because it increases the number of observed parameters, namely, polarization degree (p.d.) and position angle (p.a.) swing. So far, only the optical polarization data for the Crab pulsar is available (Smith et al. 1988; Kanbach et al. 2005) in high energy bands. For the Crab pulsar, the spectrum is continuously extending from optical to γ -ray bands. In addition, the pulse positions in the wide energy bands are all in phase, which would indicate that the optical emission mechanism is related to higher energy emission mechanisms. In the future, the next generation Compton telescope will probably be able to measure polarization characteristics in MeV bands. These data will be useful for discriminating the different models.

Chen et al. (1996) considered the polarization characteristics in the peaks of the light curve for the Crab pulsar with an outer gap model. In that model, the synchrotron radiation was used. The model assumed that the charge particles are distributed with a Gauss function in the azimuthal direction to guarantee the formation of the peaks in the light curve. Romani & Yadigaroglu (1995) calculated the polarization characteristics predicted by the curvature radiation process in the frame work of the one pole outer gap model. In that model, however, the optical polarization data of the Crab pulsar was reproduced by very specialized selection of the model parameters such as the inclination angle and the viewing angle of the observer (Dyks et al. 2004, hereafter DHR04). DHR04 showed that the two-pole caustic geometry, in which the acceleration region extends from the stellar surface to near the light cylinder, explains the pattern of the p.d. and the fast swing of the p.a. at both peaks in the light curve.

DHR04 also showed that the effect of depolarization due to overlap of the emissions from the different magnetic field lines is not strong so that the intrinsic level of the polarization degree at each radiating point remains in the bridge and off-pulse phases of the light curve. Recently, Pétri & Kirk (2005) proposed that the optical emission originates from outside the light cylinder and calculated the polarization characteristic predicted by the pulsar striped wind model (Kirk et al. 2002). However, the observations show that the pulse peaks of the radio, optical, X-ray and γ -ray are all in phase, and it is not clear how the pulsar striped wind can radiate in multi frequency. Furthermore, all of the previous models have not considered the spectrum, the light curve and the polarization all together.

In this paper, we examine the optical polarization characteristics of the Crab pulsar with the spectrum and the light curve predicted by modifying the 3-D outer gap model in CRZ00. CRZ00 has calculated the synchrotron self-inverse Compton scattering process of the secondary pairs produced outside the outer gap and has explained the Crab spectrum from X-ray to γ -ray bands. Zhang & Cheng (2002) reconsidered CRZ00 model and calculated the energy dependent light curves and the phase resolved X-ray spectrum. In CRZ00, however, the outer-wing and the off-pulse emissions of the Crab pulsars cannot be reproduced, because the traditional outer gap geometry, which extends from the null charge surface of the Goldreich-Julian charge density (Goldreich & Julian 1969) to the light cylinder along the magnetic field lines and about 180° in azimuthal direction, is assumed. Furthermore, the spectrum in the optical band was not considered. In this paper, on these grounds, we modify the CRZ00 geometrical model into a more realistic model, following recent 2-D electro-dynamical studies (Takata et al. 2004, 2006; Hirotani 2006), and we examine the light curve, the spectrum and the polarization characteristics of the Crab pulsar.

In section 2, we present the high-energy emission model and the calculation method for the polarization. In section 3, we compare the polarization characteristics in the optical band with the Crab data, and demonstrate that the present model reproduces the observed light curve, the spectrum and the polarization characteristics all together. We diagnose the viewing angle for various inclination angle and for various emission height by comparing the model with the Crab optical data. In section 4, we predict the polarization characteristics in higher energy bands.

2. EMISSION MODEL

The outline of the outer gap model for the Crab pulsar is as follows. The charge particles are accelerated by the electric field (section 2.1) parallel to the magnetic field lines in so called gap, where the charge density is different from the Goldreich-Julina charge density

(Goldreich & Julian 1969), $\rho_{GJ} \sim -\mathbf{\Omega} \cdot \mathbf{B} / 2\pi c$, where $\mathbf{\Omega}$ is the angular velocity, \mathbf{B} is the local magnetic field and c is the speed of light. The high energy particles accelerated in the gap emit the γ -ray photons (called primary photons) via the curvature radiation process. For the Crab pulsar, most of the primary photons escaping from the outer gap will convert into secondary pairs outside the gap, where the accelerating electric field vanishes, by colliding with surface and/or synchrotron X-rays emitted by the secondary pairs. The secondary pairs emit optical - MeV photons via the synchrotron process (section 2.2) and photons above MeV with the inverse Compton process. The high-energy photons emitted by the secondary pairs may convert into tertiary pairs at higher altitude by colliding with the soft X-ray from the stellar surface. The tertiary pairs emit the optical-UV photons via the synchrotron process (section 2.2.2). This secondary and tertiary photons appear as the observed radiations from the Crab pulsar. In section 3, we will show that although the observed main features of the light curve and the spectrum are explained by the emissions from the secondary pairs, the observed polarization characteristics are explained with the emissions from the tertiary pairs, which were not considered in CRZ00.

In section 2.1, we describe the outer gap structure. In section 2.2, we discuss the synchrotron emission from the secondary and the tertiary pairs. The calculation method of the polarization are described in section 2.3, In section 2.4, we introduce the model parameters of the present study.

2.1. Outer gap structure

Because the Crab pulsar has a thin gap, we describe the accelerating electric field (Cheng et al. 1986a, 1986b) with

$$E_{\parallel}(r) = \frac{\Omega B(r) f^2(r) R_{lc}^2}{cs(r)}, \quad (1)$$

where $f(r)$ is the local gap thickness in units of the light radius, $R_{lc} = c/\Omega$, and $s(r)$ is the curvature radius of the magnetic field line. This traditional outer gap model assumes that the outer gap starts from the null charge surface. However, it has been well known that the traditional outer gap geometry cannot reproduce the off-pulse emission of the Crab pulsar. On the other hand, recent 2-D electro-dynamical studies (e.g. Takata et al. 2004; Hiro-tani 2006) for the outer gap accelerator have demonstrated that the inner boundary of the outer gap is shifted toward the stellar surface from the null charge surface by the current through the gap. Therefore, we take into account the radiation and the pair-creation processes inside

the null charge surface. In such a case, the emissions between the stellar surface and the null charge surface contribute to the light curves as the outer-wing and the off-pulse emissions.

As demonstrated by the 2-D electrodynamical model, the electric field inside the null charge surface rapidly decreases along the magnetic field line because of the screening effects of the pairs produced near the inner boundary. To simulate the accelerating electric field inside null charge surface in the present geometrical study, we assume that the strength of the accelerating field changes quadratically along the magnetic field line as

$$E_{\parallel}(r) = E_n \frac{(r/r_i)^2 - 1}{(r_n/r_i)^2 - 1}, \quad r_i \leq r \leq r_n, \quad (2)$$

where E_n is the strength of the electric field at the null charge surface and r_n and r_i are the radial distances to the null charge surface and the inner boundary of the gap, respectively. For the inclined rotator, the radial distance to the null charge surface varies for different field lines so that the $r_n(\phi)$ is a function of the azimuthal angle (ϕ). In this paper, the ratio $r_i(\phi)/r_n(\phi)$ is assumed to be a constant for each field line (that is, no azimuthal dependence of r_i/r_n), and is treated as a model parameter. The local Lorentz factor of the accelerated particles (called primary particles) in the outer gap is described by $\Gamma_p(r) = [3s^2(r)E_{\parallel}/2e]^{1/4}$ with assuming the force balance between the acceleration and the curvature radiation back reaction.

The primary photons emitted in the outer gap may make the pairs inside and outside the gap with the soft X-ray from the stellar surface or the synchrotron radiation of the secondary pairs. CHRb (1986) considered the pair creation process in the gap between the primary curvature photons and the soft photons emitted by the secondary pairs, which was produced outside of the gap by the pair-creation process of the primary photons, and estimated the typical fractional gap size as $f \sim 33.2B_{12}^{-13/12}P^{33/20}$, where B_{12} is the strength of the stellar magnetic field in unit of 10^{12} G and P is the rotational period. However, the soft photons emitted from the secondary pairs may be beamed out of the outer gap, because the secondary pairs are created just outside the gap and emit the photons to the convex side of the field lines. The screening pairs will be created by the pair-creation process between the primary curvature photons and the surface X-rays. In such a case, Zhang & Cheng (1997) estimated typical fractional size of the outer gap as

$$f(R_{lc}/2) \sim 5.5B_{12}^{-4/7}P^{26/21}. \quad (3)$$

The local fractional size of the outer gap is estimated by $f(r) \sim f(R_{lc}/2)(2r/R_{lc})^{1.5}$ (CRZ00). In this paper, we use the fractional gap size $f(R_{lc}) = 0.11$ with $B_{12} = 3.7$, which is inferred from the dipole radiation model of the pulsar spin down.

The present 3-D geometrical model assumes that the outer gap extends around the whole polar cap, because we have not had any reliable model for the 3-D geometry of the acceleration region. If we consider the emission region extending very close to the light cylinder $\rho \sim R_{lc}$, the expected light curve with a moderately changing emissivity along the field line may have triple or more peaks. Therefore, we expect that the emissivity near the light cylinder is declined and/or the radiations from near the light cylinder are beamed out of line of sight due to the magnetic bending. In the calculation, we constrain the boundaries of the axial distance and radial distance for the emission regions with $\rho_{\max} = 0.9R_{lc}$ and $r = R_{lc}$, respectively.

2.2. Synchrotron emission from the pairs

2.2.1. secondary pairs

The primary photons escaping the outer gap convert into the secondary pairs by colliding the non-thermal X-ray photons, which were emitted by the synchrotron process of the secondary pairs. The photon spectrum of the synchrotron radiation by the secondary pairs is described by (CRZ00)

$$F_{syn}(E_\gamma, r) = \frac{3^{1/2}e^3B(r)\sin\theta_p(r)}{mc^2hE_\gamma} \int \left[\frac{dn_e(r)}{dE_e} \right] F(x)dE_e dV_{rad}, \quad (4)$$

where $x = E_\gamma/E_{syn}$, $E_{syn}(r) = 3he\Gamma_s^2(r)B(r)\sin\theta_p(r)/4\pi m_e c$ is the typical photon energy of the secondary pairs, Γ_s represents Lorentz factor of the secondary pairs, θ_p is the pitch angle of the particle, $F(x) = x \int_x^\infty K_{5/3}(y)dy$, where $K_{5/3}$ is the modified Bessel function of order 5/3, and dV_{rad} is the volume element of the radiation region considered. The distribution of the pairs is given by

$$\frac{dn_e}{dE_e} \sim \frac{l_{cur}n_{GJ}\ln(E_{cur}/E_e)}{\dot{E}_e E_{cur}}, \quad (5)$$

where $l_{cur} = eE_{||}c$ is the local power of the curvature radiation, $n_{GJ} = \Omega B/2\pi ce$ is the Goldreich-Julian number density, $E_{cur}(r) = 3h\Gamma_p^3(r)c/4\pi s(r)$ is the characteristic energy of the curvature photons emitted by the primary particles and $\dot{E}_e = 2e^4B^2(r)\sin^2\theta_p(r)\Gamma_s^2/3m^2c^3$ is the energy loss rate of the synchrotron radiation of the secondary pairs.

The pitch angle of the secondary pairs is estimated from $\sin\theta_p(R_{lc}) \sim \lambda/s(R_{lc})$, where λ is the mean free path of the pair-creation between the primary γ -rays and the non-thermal X-rays from the secondary pairs. The mean free path is estimated from $\lambda^{-1} \sim n_X\sigma_{\gamma\gamma}$, where n_X is the typical non-thermal X-ray number density and $\sigma_{\gamma\gamma}$ is the pair-creation cross section, which is approximately given by $\sigma_{\gamma\gamma} \sim \sigma_T/3$, where σ_T is the Thomson cross section. For

the Crab pulsar, the typical number density becomes $n_X \sim L_X(\langle E_X \rangle)/\delta\Omega R_{lc}^2 c \langle E_X \rangle \sim 8 \times 10^{17} \text{ cm}^{-3}$, where we used the typical energy $\langle E_X \rangle \sim (2m_e c^2)^2/10 \text{ GeV} \sim 100 \text{ eV}$, the typical non-thermal X-ray luminosity $L_X \sim 10^{35} \text{ erg/s}$, and the solid angle $\delta\Omega = 1$ radian. As a result, the mean free path becomes $\lambda \sim 10^7 \text{ cm}$ so that the pitch angle is estimated by $\sin \theta_p \sim \lambda/s(R_{lc}) \sim 0.06$, where we used the curvature radius $s(R_{lc}) = R_{lc}$. In this paper, therefore, we adopt $\sin \theta_p(R_{lc}) = 0.06$. The local pitch angle is calculated from $\sin \theta_p(r) = \sin \theta_p(R_{lc})(r/R_{lc})^{1/2}$.

The outer gap extends above the last-open lines with the thickness $f(R_{lc})$. And then, we assume that the secondary pair region extends just above the outer gap with the thickness λ .

2.2.2. tertiary pairs

Some high-energy photons emitted by the inverse Compton process of the secondary pairs may convert into tertiary pairs at higher altitude by colliding with thermal X-ray photons from the star. The energy of the new born tertiary pairs will be described by the most energetic secondary photons from the secondary pairs. According to the study by CRZ00, the most energetic ($\sim 1 \text{ GeV}$) secondary photons via the inverse Compton process of the secondary pairs are about one order magnitude smaller than that of the primary photons ($\sim 10 \text{ GeV}$), which make the secondary pairs. Therefore, we expect that the tertiary pairs are produced with a Lorentz factor of one order magnitude smaller than that of the secondary pairs. The optical depth of the pair-creation between the high-energy photons emitted by the secondary pairs and the thermal X-ray photons from the stellar surface is estimated as $\tau \sim n_X \sigma_{\gamma\gamma} R_{lc} \sim 0.1$, with the typical thermal X-ray number density $n_X \sim 4\pi R_*^3 \sigma T^4 / 4\pi R_{lc}^2 c k_B T \sim 5 \times 10^{15} \text{ /cm}^3$, where $R_* = 10^6 \text{ cm}$ is the stellar radius, σ is the Stefan-Boltzmann constant, k_B is the Boltzmann constant, and T is the surface temperature, for which we adopt the reasonable value $T = 2 \cdot 10^6 \text{ K}$ (Yakovlev & Pethick 2004). In this paper, therefore, we use that the maximum energy of and the local number density of the tertiary pairs are smaller than about 10% of those of the secondary pairs. Because the pitch angle of the pairs increases with altitude, we use $\sin \theta_p = 0.1$ for the pitch angle of the tertiary pairs. In fact, the results are not sensitive to the pitch angle of the tertiary pairs.

The tertiary pairs are produced above the region of the secondary pairs. As we will see in section 3.1, the emissions from the secondary pairs make the main features of the light curve such as the two peaks in a period, and the emissions from the tertiary pairs contribute to the bridge phase.

2.2.3. *synchrotron cooling*

For the Crab pulsar, the observed spectrum has a spectral break around 10 eV. This feature was not considered in CRZ00. One possibility of the explanation of the observed break is due to the effect of the synchrotron cooling. The damping length due to the synchrotron cooling is given by $l_{syn} \sim 3 \cdot 10^4 (B/10^7 \text{G})^{-2} (\Gamma_{\perp}/10^2)^{-1} (\sin \theta_p/0.06)$ cm, where $\Gamma_{\perp} = \Gamma/\Gamma_{\parallel}$ and $\Gamma_{\parallel} = 1/\sin \theta_p$. The charge particles quickly lose their perpendicular momentum via the synchrotron radiation. The minimum Lorentz factor of the pairs in the magnetosphere may be described by $\Gamma \sim \Gamma_{\parallel} \sim 17$, which is corresponding to the synchrotron characteristic energy $E_c \sim 3(\Gamma/17)^2 (B/10^7 \text{G}) (\sin \theta_p/0.06)$ eV. In the present model, therefore, the spectral index s_{ν} of the synchrotron photons varies from $s_{\nu} = (p-1)/2$ with $p = 2$ of equation (5) in X-ray bands to $s_{\nu} \sim -1/3$, which is reflecting the single particle emissivity, below the energy E_c .

2.2.4. *emission direction of the pairs*

We use the rotating dipole field in the inertial observer frame (hereafter IOF). On the other hand, the previous works such as CRZ00 and DHR04 used the rotating dipole field in the co-rotating frame, in which the emission direction coincides with the local magnetic field direction, and performed the Lorentz transformation to calculate the emission direction in IOF. As a result, the configuration of the magnetic field in IOF is different between the present model and the previous works, although the difference is small except for near the light cylinder.

For a high Lorentz factor, we can anticipate that the emission direction of the particles coincides with the direction of the particle's velocity. In IOF, the motion of the pairs created outside of the gap may be described by

$$\mathbf{n} = \beta_0 \cos \theta_p \mathbf{b} + \beta_0 \sin \theta_p \mathbf{b}_{\perp} + \beta_{co} \mathbf{e}_{\phi}, \quad (6)$$

where the first term in the right hand side represents the particle motion along the field line, $\mathbf{b} = \mathbf{B}/B$ (or $-\mathbf{B}/B$) for the particles migrating parallel (or counter parallel) to the direction of the magnetic field. In this paper, we consider only outgoing particles because the photons emitted by ingoing particles will be much fainter than that by the outgoing particles (CRZ00). The second term in equation (6) represents gyration motion around the magnetic field line and the third term is co-rotation motion with the star, $\beta_{co} = \rho\Omega/c$. The unit vector \mathbf{b}_{\perp} perpendicular to the magnetic field line becomes

$$\mathbf{b}_{\perp} \equiv \pm(\cos \delta\phi \mathbf{k} + \sin \delta\phi \mathbf{k} \times \mathbf{b}), \quad (7)$$

where \pm represents the gyration of the positrons (+) and the electrons (-), $\delta\phi$ refers the phase of gyration motion and $\mathbf{k} = (\mathbf{b} \cdot \nabla)\mathbf{b}/|(\mathbf{b} \cdot \nabla)\mathbf{b}|$ is the unit vector of the curvature of the magnetic field lines. The gyration phase $\delta\phi$ is defined so that the value increases in the direction of the gyration motion of the positrons and so that the pairs with $\delta\phi = 0$ emit the photons in the plane spanned by the directions of the local magnetic field and its curvature if there were no co-rotation motion in equation (6). The co-rotation motion affects the emission direction as the aberration effect. The value of β_0 at each point is determined by the condition that $|\mathbf{n}| = 1$.

The emission direction of equation (6) is described in terms of the viewing angle measured from the rotational axis, $\xi = \cos^{-1} n_z$, and the rotation phase, $\Phi = -\Phi_n - \mathbf{r} \cdot \mathbf{n}$, where n_z is the component of the emission direction parallel to the rotational axis, Φ_n is the azimuthal angle of the emission direction and \mathbf{r} is the emitting location in units of the light radius.

Because the particles distribute on the gyration phase $\delta\phi$, the emitted beam at each point must become cone like shape with opening angle $\theta_p(r)$. For each radiating point, the emission directions of the different particles on the gyration phase are projected onto the different points in (ξ, Φ) plane. Furthermore, the polarization plane of the radiations also depends on the gyration phases of the radiating particles. Taking into account the dependence on the gyration phase, therefore, we calculate the radiations from the particles for all of the gyration phase $\delta\phi = 2\pi i/n$ ($i = 1, \dots, n - 1$). Figure 1 shows the emission projection onto (ξ, Φ) plane for different gyration phases ($\delta\phi = 0^\circ, 90^\circ, 180^\circ$ and 270°) for the positrons. For the electrons, we find from the equation (7) that the emission projection map of the electrons is identical with Figure 1 but the gyration phase is different by 180° ; for example, the panels for $\delta\phi = 0^\circ$ and 90° for the positrons in Figure 1 also describe the projection maps of emission from the electrons with $\delta\phi = 180^\circ$ and 270° , respectively.

With the projection map of the emissions, the expected pulse profile is determined by choosing the viewing angle ξ of the observer and collecting all photons from the possible emitting points and the gyration phases with the emissivity of equation (4).

2.3. The Stokes parameters

We assume that the radiation at each point linearly polarizes with degree of $\Pi_{syn} = (p + 1)/(p + 7/3)$, where p is the power law index of the particle distribution, and circular polarization is zero, that is, $V = 0$ in terms of the Stokes parameters. The direction of the electric vector of the electro-magnetic wave toward the observer is parallel to the projected

direction of the acceleration of the particle on the sky (Blaskiewicz et al. 1991). The magnitude of the microscopic acceleration of the gyration motion is much larger than that of the macroscopic acceleration of the co-rotation motion so that the ratio of the magnitude of the two accelerations becomes $\omega_B/\Omega \sim 10^8(B/10^6\text{G})(\Gamma/10^3)^{-1}$, where ω_B and Ω are the gyration and the co-rotation frequencies, respectively. Unless the pitch angle is very small, the acceleration with equation (6) is approximately written by

$$\mathbf{a} \sim \beta_0 \omega_B \sin \theta_p (-\sin \delta \phi \mathbf{k} + \cos \delta \phi \mathbf{k} \times \mathbf{b}). \quad (8)$$

The electric vector \mathbf{E}_{em} emitted in the direction \mathbf{n} becomes $\mathbf{E}_{em} \propto \mathbf{a} - (\mathbf{n} \cdot \mathbf{a})\mathbf{n}$.

To calculate the Stokes parameters Q^i and U^i for each radiating point, we define the position angle χ^i to be angle between the electric field \mathbf{E}_{em} and the projected rotational axis on the sky, $\mathbf{\Omega}_p = \mathbf{\Omega} - (\mathbf{n} \cdot \mathbf{\Omega})\mathbf{n}$. The Stokes parameters Q^i and U^i at each radiation is represented by $Q^i = \Pi_{syn} I^i \cos 2\chi^i$ and $U^i = \Pi_{syn} I^i \sin 2\chi^i$, where I^i is the intensity. After collecting the photons from the possible points for each rotation phase Φ and a viewing angle ξ , the expected p.d. and p.a. are, respectively, obtained from

$$P(\xi, \Phi) = \Pi_{syn} \frac{\sqrt{Q^2(\xi, \Phi) + U^2(\xi, \Phi)}}{I(\xi, \Phi)}, \quad (9)$$

and

$$\chi(\xi, \Phi) = 0.5 \text{atan} \left[\frac{U(\xi, \Phi)}{Q(\xi, \Phi)} \right], \quad (10)$$

where $Q(\xi, \Phi) = \Sigma Q^i$ and $U(\xi, \Phi) = \Sigma U^i$ are the Stokes parameters after collecting the photons.

Finally, we describe the difference between polarization characteristics predicted by the curvature emission and synchrotron emission models. If we ignore the effects of the aberration due to the co-rotation motion, the direction of the electric vector of the wave for the curvature and synchrotron cases are, respectively, parallel to and perpendicular to the magnetic field projected on the sky (Rybicki & Lightman 1979). Secondly, in the curvature radiation model the photons are radiated only one direction at each point, which coincides with the direction of the local magnetic field line if we ignore the aberration effect. Furthermore, the radiations from neighboring positions polarize in similar directions. In such a case, the intrinsic level of the polarization degree at the each radiating point remains in the bridge and off-pulse phase of the light curve (DHR04). Therefore, to explain the observed polarization degree $\sim 10\%$ at the bridge phase of the Crab pulsar, the curvature emission model may require the radiation linearly polarized with about 10% at each radiating points. As we have mentioned for the synchrotron case, on the other hand, the photons are emitted along the surface of the cone with opening angle θ_p at each radiating position. Furthermore, the polarization plane

of the radiation depends on the gyration phase of the radiating particle. In such a case, the observed radiation consists of the radiations from the different particles on the gyration phase. This overlap of the radiations causes a strong depolarization, and as a result a lower polarization degree is expected for the synchrotron case. We need not assume the radiations with a low polarization degree at each radiating point to explain the Crab data. In the present model, the intrinsic polarization degree of the radiation at the each radiating point is $\sim 70\%$ using the particle distribution $p = 2$ described by equation (5).

2.4. Model parameters

In this subsection, we introduce the model parameters. The inclination angle α and the viewing angles ξ measured from the rotational axis are the model parameters. Because the inner boundary of the outer gap is determined by the current through the gap (Takata et al. 2004), we consider the position of inner boundary located inside of the null charge. In this paper, the ratio of the radial distances to the inner boundary r_i and the null charge surface of the rotating dipole r_n , which is a function of the azimuthal angle, is treated as a model parameters, and is assumed to be constant for each field line as described in section 2.1.

Since the magnetic field must be modified by the rotational and the plasma effects near the light cylinder, the last-open field line must be different with the traditional magnetic surface that is tangent to the light cylinder for the vacuum case. For example, Romani (1996) defined the last open lines as the field lines parallel to the rotational axis at $r = R_{lc}/2^{1/2}$, where the corotational velocity equals the Alfvén speed. To specify the gap upper surface, therefore, it is convenient to refer the footpoints of the magnetic field lines on the stellar surface. With the assumption that the gap upper surface coincides with a magnetic surface, we parameterize the fractional polar angle $a = \theta_u/\theta_{lc}$, where θ_u is the polar angle of the footpoints of the magnetic field lines of the gap upper surface and θ_{lc} is the polar angle of the field lines which are tangent to the light cylinder for the vacuum case.

Finally, we describe how the model parameters (α , ξ , r_i and a) are diagnosed by the present model and the Crab data. The model parameters are chosen so that the expected light curve, the spectrum and the polarization characteristics are simultaneously consistent with the Crab data such as the phase separation $\delta\Phi \sim 0.4$ phase between two peaks and the large position angle swings at the both peaks. As we will demonstrate in section 3.1, the features of the expected light curve is sensitive to the viewing angle ξ but not to the position of the inner boundary r_i , if we fix the inclination angle α and the fractional angle a . Therefore, the viewing angle ξ is determined by comparing the model and the observed light curves. With the determined viewing angle, on the other hand, the radial distance to

the inner boundary r_i affects sensitively to the polarization characteristics at the off-pulse phase. Therefore, if the inclination angle α and the gap upper surface a are determined in some way, the viewing angle ξ of the observer and the position of the inner boundary of the outer gap r_i are diagnosed by the present model and the Crab data. The present geometrical model produces a consistent spectrum with the Crab data (section 3.2) using the viewing angle determined from the observed light curve. We need not introduce another model parameter for fitting the spectrum. It is difficult to constrain both the inclination angle α and the upper surface a with the present model. As we will show in section 3.4.3, however, if either inclination angle α or the altitude of the upper surface a is determined in some way, the other may be diagnosed by the present model.

3. RESULTS

3.1. Light curve

Figure 2 compares the polarization characteristics at 1 eV predicted by three different emission geometries. The left column summarizes the results for the traditional outer gap geometry, in which the inner boundary of the gap is located at the null charge surface of the Goldreich-Julian charge density. Although the traditional model in CRZ00 and the present model assume the different extensions of the outer gap in the azimuthal direction, that is around half (in CRZ00) and whole (in the present model) polar-cap region, we find that the predicted polarization characteristics are not so different between the two azimuthal extension of the outer gap geometries as long as the inner boundary is located at the null charge surface. In this section, therefore, the gap geometry that starts from the null charge surface and extends around whole polar cap region is also called as "traditional geometry".

The middle and right in Figure 2 columns show the results for the radial distance of 67% of the distance to null charge surface $r_i = 0.67r$, and the right column is taking into account also the emissions from the tertiary pairs. The other model parameters are $\alpha = 50^\circ$, $a = 0.94$, and $\xi \sim 100^\circ$, where the viewing angle is chosen so that the predicted phase separation between the two peaks is consistent with the observed value $\delta\Phi \sim 0.4$ phase. In the figure, we define zero of the rotation phase at the main peak.

By comparing the pulse profiles between the light curves of the left and middle columns, we find that the radiations from the secondary pairs inside the null charge surface contribute to the outer-wing and the off-pulse emissions. In the present case, the off-pulse emissions are $< 10^{-1}\%$ of the peak flux, because the line of sight marginally passes through the emission regions in the off-pulse phase as the horizontal lines show in Figure 1. Near the inner

boundary, because the accelerating electric field and resultant the energy of emitted primary photons in the gap are small, the secondary pairs are produced with a lower energy, and emit the synchrotron photons with a smaller emissivity.

As Figure 1 indicates, the emerging radiations in the light curve originate from the two poles; one pole contributes to the light curve with the two peaks and the bridge photons emitted beyond the null charge surface, and the other contributes with the outer-wing and the off-pulse photons emitted inside the null charge surface. Dyks & Rudak (2003) have proposed the radiations associated with two magnetic pole. In that model, with the constant emissivity along the magnetic field lines, the two peaks are associated with the different poles and the different emission regions, and are formed by the caustic effect near the stellar surface. In the present outer gap model, on the other hand, the electric field, and the resultant emissivity of the synchrotron radiation of the secondary pairs quickly decreases inside the null charge surface. Therefore, although the caustic effect near the stellar surface is strong, the emissions inside the null charge surface do not make a strong peak compared with the present main peak, which is formed by the radiations near the light cylinder. In the present case, therefore, the two peaks in the light curve is associated with the one magnetic pole.

By comparing the flux levels of the bridge emissions between the light curves in the middle and right columns, we find that the tertiary pairs mainly contribute to the emissions at the bridge phase. This is because the tertiary pairs are born and emit photons at higher altitude than the secondary pairs, which make two peaks in the light curve.

3.2. Polarization

Middle and lower panels in Figure 2 show the predicted polarization position angle (p.a.) and the polarization degree (p.d.), respectively. For reference, the light curve is overplotted in each frame.

As seen in the polarization characteristics by the traditional model, we find that the secondary emissions beyond the null charge surface make the polarization characteristics such that the polarization degree takes a lower value at the bridge phase and a larger value near the peaks. In the synchrotron case, the cone like beam is radiated at each point, and an overlap of the radiations from the different particles on the gyration phase causes the depolarization. For the viewing angle $\xi \sim 100^\circ$, the radiations from all gyration phases contribute to the observed radiation at the bridge phase as the vertical dotted lines at $\Phi = 0.2$ phase in Figure 1 show. In such a case, the depolarization is strong, and as a result, the emerging radiation from the secondary pairs polarizes with a very low p.d. ($< 10\%$).

Near the peaks, on the other hand, the radiations from the some gyration phase are not observed as the vertical dotted-dashed lines in Figure 1 show. For example, the observer with the viewing angle $\xi \sim 100^\circ$ detects the photons from the gyration phase $\delta\phi = 0^\circ$ at the rotation phase $\Phi = 0.4$ phase (second peak), but does not detect from $\delta\phi = 180^\circ$. In such a case, the depolarization is weaker and the emerging radiation highly polarizes.

As the polarization degrees in the middle and right columns in Figure 2 show, the radiations from the inside the null charge surface may be observed with a large polarization degree at the off-pulse phase. This is because the line of sight $\xi \sim 100^\circ$ passes through marginally the edge of the radiating region with $r_i = 0.67r_n$ at the off-pulse phase as horizontal lines in Figure 1 show. The observer can not detect the radiations from the particles within a range of the gyration phase; for example, at the rotational phase $\Phi = 0.6$ phase (off-pulse phase) in Figure 1, the observer with viewing angle $\xi \sim 100^\circ$ detects the radiations from the particles with the gyration phases $\delta\phi = 180^\circ$ and $\delta\phi = 270^\circ$, but does not with $\delta\phi = 0^\circ$ and $\delta\phi = 90^\circ$. In such a case, the depolarization in the off-pulse phase is weak and the expected p.d. exhibits a larger value. Actually, as we will show in section 3.4.2, the p.d. at the off-pulse phase is sensitive to the position of the inner boundary r_i .

We can see the effects of the tertiary pairs on the polarization characteristics at the bridge phase. By comparing the p.d. between middle and right panels, we find that tertiary pairs produce the radiations with $\sim 10\%$ of the p.d. at the bridge phase.

3.3. Comparison with observations

Figure 3 compares the predicted polarization characteristics at 1 eV with the Crab optical data. Left and middle columns are, respectively, the Crab optical data for the total emissions and for the emissions after subtraction of the DC level, which has the constant intensity at the level of 1.24% of the main pulse intensity (Kanbach et al. 2005).

In the total emissions (left column), the impressive polarization feature from the Crab pulsar is that the off-pulse and bridge phases have the fixed value of the p.a. These polarization features of the observation are not predicted by the present model, which predicts about 90° difference on the p.a. between the off-pulse and the bridge phases as the right column shows.

The constant p.a. in the total emissions may suggest that the Crab optical emissions consist of two components, that is, constant and pulsed components. The DC level emissions may include both the magnetospheric component and the background components (e.g. the pulsar wind and the nebula components). After the subtraction of the DC level, the large

p.a. swings larger than $\sim 100^\circ$ appears at the both peaks, and the constancy of the p.a. at both bridge and off-pulse phase disappears. We can see that the polarization characteristics predicted by the present model are more consistent with the Crab optical data after the subtraction of the DC level. Especially, the model reproduces the most striking feature in the observed p.a. that the large swing at both peaks, and the observed low p.d. at bridge phase $\sim 10\%$. Also, the pattern of the p.d. are reproduced by the present model.

In the off-pulse phase, it is not clarified that which radiation component, that is, the magnetospheric or back ground (e.g the pulsar wind and nebula components) components dominates the other one at the off-pulse phase, where the flux level of the magnetospheric component is much smaller than the peak flux. Furthermore, the data for emissions after subtraction of the DC level has a few photons in the off-pulse phase so that the polarization behavior in the off-pulse phase may not be determined. The present model (e.g. the polarization characteristics in the right column in Figure 2) predicts that radiation from the magnetospheric component at the off-pulse phase has a relatively constant position angle, which is about 90° difference from that in the bridge phase. This constancy of the p.a. in the off-pulse phase is not sensitive to the model parameters such as the viewing angle ξ and the position of the inner boundary r_i (Figures 5 and 7).

Although the present model has successfully explained the main features of the Crab optical polarization data, it also has some disagreements with the Crab data. For example, the model predicts the small p.a. swing at the leading-wing of the second peak before appearing the large p.a. swing at the second peak. In the p.d., furthermore, the another peaks in the p.d. at both peaks are predicted.

Figure 4 compares the model spectrum with the Crab data in optical-MeV bands. The model parameters are same with that in the right column in Figure 3. In this case. we assume that the pairs escape from the light cylinder with the Lorentz factor $\Gamma \sim 17$ (section 2.2.3), which predicts the spectral break around 10 eV. The model spectrum also explains the general features of the data. Therefore, the outer gap model can explain the general features of the observed light curve, the spectrum and the polarization characteristics in optical band for the Crab pulsar, simultaneously.

3.4. Dependence on the model parameters

In this section, we discuss the dependence of the polarization characteristics on the model parameters and diagnose that for the Crab pulsar.

3.4.1. viewing angle

Figure 5 summarizes the dependence of the polarization characteristics on the viewing angle. With $\alpha = 50^\circ$, $a = 0.94$ and $r_i = 0.67r_n$, the left, middle and right columns show, respectively, the polarization characteristics for the viewing angle of $\xi \sim 95^\circ$, $\xi \sim 100^\circ$ and $\xi \sim 105^\circ$. For $\xi \sim 100^\circ$, the phase separation of the two peaks in the light curve is $\delta\Phi \sim 0.4$ phase similar with the observation.

We can see that the phase separation becomes wider (or narrower) with decreasing (of increasing) the viewing angle from $\xi \sim 100^\circ$. For example, as the light curve of the left column shows, the phase separation between two peaks for $\xi \sim 95^\circ$ becomes obviously wider than $\delta\Phi \sim 0.4$ phase. On the other hand, the phase separation for $\xi \sim 105^\circ$ becomes narrower than the data. Furthermore, in the light curve for $\xi \sim 105^\circ$, we can see a conspicuous peak in the leading-wing of the main peak. This leading small peak is formed by the radiations inside the null charge surface of the radiation region connecting to the other pole, while the main peak is formed by the radiations near the light cylinder. For $\xi \sim 95^\circ$ and $\sim 100^\circ$, these two peaks are observed as a single main peak, because the phase separation of the two peaks is very narrow.

By comparing the p.d. for three cases, we find that p.d. in off-pulse phase increases with the viewing angle; e.g. typical p.d. in the off-pulse phase is $\sim 20\%$ for $\xi \sim 95^\circ$ and $\sim 60\%$ for $\xi \sim 100^\circ$. As we have mentioned in section 3.2, the present model predicts highly polarized radiations at the off-pulse phase, if the line of sight marginally passes through the emission region. Increasing the viewing angle with a specific position of the inner boundary r_i , the line of sight approaches the inner boundary from inside the emission region as we can expect from Figure 1, and then the radiations from wider range of the gyration phases become to be beamed out of the line of the sight. Therefore, the p.d. in off-pulse phase increases with the viewing angle. Finally, if the line of sight passes through outside the emission region, there are no emissions in the off-pulse phase such as the light curve of the right column in Figure 5.

As we have seen, the viewing angle affects sensitively to the model light curve and the polarization degree in the off-pulse phase. In the present model, especially, the observed phase separation of the two peaks $\delta\Phi \sim 0.4$ restricts the viewing angle with $\pm 5^\circ$ uncertainty.

Let us consider the two viewing angles mutually symmetric with respect to the rotational equator (e.g. the viewing angles 80° and 100°). For such symmetric viewing angles, the light curves, the spectra and the p.d. curves are identical. However, the p.a. curves are mirror symmetry with respect to the rotational equator because of the difference directions of the projected magnetic field on the sky. Figure 6 shows the polarization position angles for the

viewing angles $\xi \sim 80^\circ$ (left column) and $\xi \sim 100^\circ$ (right column) with $\alpha = 50^\circ$, $a = 0.94$ and $r_i = 0.67r_n$. By comparing the swing pattern at the both peaks between the model results in Figure 6 and the data in Figure 3, we find that the p.a. for $\xi \sim 100^\circ$ is more consistent with the Crab data. The behavior of the p.a. swing does not change for different viewing angles in the same hemisphere. Therefore, the viewing angle larger than 90° are preferred for the Crab pulsar.

Although we can distinguish the two viewing angle mutually symmetric with respect to the rotational equator, the present model does not allow to distinguish the two inclination angles mutually symmetric with respect to the rotational equator, that is, α and $180^\circ - \alpha$. This is because the present model has considered the only outgoing electron and positron pairs. We have not used the information of the magnetic polarity for the emissions from the pairs.

3.4.2. inner boundary, r_i

We consider the dependence of the polarization characteristics on the position of the inner boundary of the outer gap by fixing the inclination angle, $\alpha = 50^\circ$, the gap upper surface $a = 0.94$ and the viewing angle $\xi \sim 100^\circ$. As mentioned in section 2.1, we assume the ratio of the radial distances to the inner boundary and the null charge surface, $r_i(\phi)/r_n(\phi)$, is not a function of the azimuthal angle ϕ , although $r_n(\phi)$ and $r_i(\phi)$ depend on the azimuthal angle.

Figure 7 summarizes the polarization characteristics for $r_i = 0.60r_n$ (right column), $0.67r_n$ (middle column) and $0.74r_n$ (right column). From Figure 7, we find that the position of the inner boundary hardly affects the expected light curve. This is because the radiations from inside of the null charge surface contribute to the off-pulse emissions with a small flux (Figure 2).

From Figure 7, we find that the p.d. in the off-pulse phase increases with shifting the inner boundary from the stellar surface toward the null charge surface; e.g. typical p.d. in the off-pulse phase is $\sim 30\%$ for $r_i = 0.60r_n$ and $\sim 60\%$ for $r_i = 0.67r_n$. The reason of the increase is the same with the results in section 3.4.1, where we discussed the dependence of the viewing angle ξ with a fixed position of the inner boundary r_i . In the present case, the line of sight $\xi \sim 100^\circ$ passes through the radiating points of $r \sim 0.7r_n$ in the off-pulse phase. In such a case, for $r_i = 0.6r_n$ the observer detects the photons from most of all gyration phase, and emerging radiation polarizes with a low p.d. For $r_i = 0.67r_n$, on the other hand, the line of sight passes through near the inner boundary and therefore, the radiation at off-

pulse phase appears with a large p.d as discussed in 3.4.1. For $r_i = 0.74r_n$ (right column), the line of the sight passes through outside the emission region at the off-pulse phase.

In the middle panels for each column, we see that the main features of the p.a. (e.g. the large swings at both peaks) do not depend the position of the inner boundary. Therefore, the dependence of the position of the inner boundary mainly appears as the difference of the p.d. at the off-pulse phase. In the observation, however, both the emissions from the magnetosphere and the back ground (e.g. the wind region, and probably nebula) components would contribute to the off-pulse emissions. It is not clear which component dominates the emissions in the off-pulse phase, while the magnetospheric component must dominate in the pulse and the bridge phases. To constrain the inner boundary of the emission region with the present magnetospheric radiation model, the model requires the data of the p.d. of the off-pulse emissions from the magnetosphere. If the p.d. of the magnetospheric component are measured at the off-pulse phase, the present model will be able to restrict the radial distance of the inner boundary better. Furthermore, we may be able to diagnose how large current runs through the gap with the present geometrical model and the Crab optical data, because the position of the inner boundary of the gap is related to the current through the gap (Takata et al. 2004).

As we have seen in sections 3.4.1 and 3.4.2, the polarization characteristics are sensitive to the both viewing angle ξ and the position of the inner boundary r_i , on the other hand, the expected light curve is sensitive to only the viewing angle ξ . Therefore, the viewing angle is restricted by the observed light curve rather than the polarization characteristics. With the viewing angle determined by the light curve, the position of the inner boundary is restricted by the polarization characteristics.

3.4.3. *inclination angle and gap upper surface*

As we have shown in sections 3.4.1 and 3.4.2, if the inclination angle and the altitude of the gap upper surface could be determined, the viewing angle ξ are restricted by the observed light curve, and then the position of the inner boundary of the gap r_i are determined by the Crab optical polarization data. In this section, we examine how ξ and r_i for explaining the Crab data are changing with the inclination angle α and the altitude of the gap upper surface (in other words the fractional angle a), above which the secondary pairs are produced and the emit the observed photons. For each inclination angle α and the altitude of the gap upper surface a , the viewing angle ξ is chosen to explain the observed characteristics that the light curve has two peaks, first peak is stronger than the second peak (in optical band) and the phase separation between two peaks is ~ 0.4 phase. The position of the inner boundary

r_i is determined so that the p.a. has a large swings at the both peaks, and the p.d. in the off-pulse phase becomes about $\sim 60\%$ because we do not have accurate data of the p.d. for the magnetospheric radiations at the off-pulse phase.

Table 1 summarizes the expected viewing angle ξ and the radial distance to the inner boundary r_i for the inclination angles $\alpha = 40^\circ, 50^\circ$ and 60° and the various altitude of the gap upper surface. In the table, the increasing of the value of the fractional angle a means the decreasing of the altitude of the upper surface of the gap with $f(R_{lc}) = 0.11$, and of the emissions region of the secondary pairs. We find that there is a critical altitude of the upper surface ($\equiv a_c$) for each inclination angle; e.g $a_c \sim 0.91$ for $\alpha = 40^\circ$, $a_c \sim 0.93$ for $\alpha = 50^\circ$ and $a_c \sim 0.95$ for $\alpha = 60^\circ$. With a fractional angle a smaller than the critical value (in other words, with a higher upper surface than the critical altitude), there are no viewing angle that produces the light curve consistent with data, and the expected light curve has triple peaks (leading peak, main peak and second peak) such like the light curve in the right column of Figure 5.

For a specific inclination angle α , the expected viewing angle ξ increases with decreasing the altitude of the gap upper surface (or with the increasing the fractional angle a). The reason is explained as follows. Firstly, the phase separation of the two peaks increases with decreasing emission height because the area of the magnetic surface for the radiation regions becomes wider for lower altitude; for example, the viewing angle $\xi \sim 100^\circ$ produces the phase separation $\delta\Phi \sim 0.4$ phase in the light curve with $\alpha = 40^\circ$ and $a = 0.91$, and therefore predicts a wider phase separation of the two peaks than $\delta\Phi = 0.4$ phase for $a = 0.92$. Secondly, the phase separation of the two peaks becomes narrower with increasing the viewing angle as shown in Figure 5. As a result, the suitable viewing angle $\xi \sim 102.5^\circ$ of $a = 0.92$ is larger than $\xi \sim 100^\circ$ of $a = 0.91$.

We also find that the critical altitude of the upper surface decreases when the inclination angle α increases. As we have discussed in section 3.1, if the phase separation between the main peak and the small leading peak, which originates of the emissions inside null charge surface, is enough narrow, these two peaks appear as a single main peak in the light curve. If it is not, the light curve has a small peak in the leading-wing of the main peak. With a fixed altitude of the upper surface a , greater inclination angle α produces a wider phase separation between the main peak and the leading small peak. On the other hand, a lower altitude of the emission region with a fixed inclination angle produces a narrower phase separation of the two peaks. As a result, to have a single main peak without the leading small peak, a lower altitude of the emission regions of the secondary pairs, in other words, a larger value of the fractional angle a of the gap upper surface is required for a greater inclination angle α .

The position of the inner boundary r_i , which is chosen so that the p.d. at the off-pulse phase becomes $\sim 60\%$, approaches to the stellar surface with decreasing (or increasing) of the altitude of the gap upper surface (or the fractional angle a). As we discussed in the third paragraph of this section, a larger viewing angle ξ is preferred for explaining the phase separation of the two peaks for a lower altitude of the gap upper surface. And, the larger viewing angle (for $\xi > 90^\circ$) detects the photons emitted from the positions nearer the stellar surface. Therefore, the inner boundary is shifted toward stellar surface to hold a constant p.d. at the off-pulse phase with decreasing (or increasing) of the altitude of the upper surface (or the fractional angle a).

Finally, the present local model cannot identify the inclination angle α and the altitude of the upper gap surface, where may be determined by the observation or other ways. However if either the inclination angle or the gap upper surface is determined, the present model can constrain the other one; for example, if the inclination angle of $\alpha \sim 50^\circ$ were determined, the Crab pulsar should have the gap upper surface, which is located at lower altitude than that referred by $a \sim 0.93$. If the inclination angle α and the altitude of the upper surface are determined, the viewing angle ξ and the position of the inner boundary r_i are determined by the observed light curve and the polarization characteristics as we discussed in sections 3.4.1 and 3.4.2.

4. SUMMARY & DISCUSSION

We have considered the light curve and the spectrum for the Crab pulsar predicted by the outer gap model which takes into account the emissions from the inside the null charge surface and from the tertiary pairs. We have also calculated the polarization characteristics in the optical band. We have shown that the emissions from the inside the null charge surface contribute to the outer-wing and the off-pulse phase. On the other hand, the radiations from the tertiary pairs contribute to the bridge emissions of the light curve. We find that the expected polarization characteristics are consistent with the Crab optical data after subtraction of the DC level. The general features of the polarization characteristics, the light curve and the spectrum in optical bands have been reproduced simultaneously. For the Crab pulsar, the observed position angle swing indicates that the viewing angle of the observer measured from the rotational axis is greater than 90° .

Although the present model has explained the observed light curve, spectrum and the polarization characteristics in the optical band for the Crab pulsar, we also find that the small peak, which leads the main peak and originates from the emissions inside null charge surface, becomes to be conspicuous with increasing the energy bands if we fixed the model

parameters to produce the phase separation $\delta\Phi \sim 0.4$ phase between the main and the second peaks. The main peak consists of the radiations from the near the light cylinder, while the leading peak consists of the radiations near the stellar surface. The spectrum of the photons of the leading peak becomes harder than that of the main peak, because the magnetic field near the stellar surface is much stronger than that near the light cylinder. The flux ratio of the leading peak and the main peak decreases with increasing the energy bands. As a result, the expected light curve in higher energy bands may have triple peaks although the light curve in the optical has only two peaks.

If we are allowed a small discrepancy on the phase separation between the main and the second peaks with the Crab data $\delta\Phi \sim 0.4$, the present model can successful explain the general features of other observed features. Figure 8 summarizes the results for the viewing angles $\xi \sim 95^\circ$ and $r_i = 0.85r_n$ with the inclination angle $\alpha = 50^\circ$ and the gap upper surface of $a = 0.94$. We see that although the phase separation $\delta\Phi \sim 0.45$ phase of the two peaks is slightly larger than $\delta\Phi \sim 0.4$ phase for the Crab pulsar, the leading peak originating from the emissions near the stellar surface keeps a low profile in the light curves in wide energy bands. Furthermore, we note that the model light curves reproduce the energy dependent features of the observed light curves that the flux levels of the second peak and bridge phase increase relative to that of the main peak, and the flux levels of the two peaks become to be the same at around 10 keV (Kuiper et al. 2001). Because the phase separation of the main and the second peaks depends on the configuration of the magnetic field, the present results may predict that actual magnetic field in the pulsar magnetosphere is modified on some level from the vacuum dipole field, which has been assumed in the present paper, by the plasma effects (Muslimov & Harding 2005).

From Figure 8, we can see that the polarization characteristics depend on the energy bands. Especially, the polarization degree in the bridge phase decreases from about 10% in optical band with increasing the energy bands. In the optical band, the tertiary pairs contribute to the bridge emissions with about 10% of the p.d. For higher energy bands, on the other hand, the emissions from the secondary pairs dominate in the bridge phase, because the tertiary pairs contribute to the bridge emissions with a smaller Lorentz factor and emissivity via the synchrotron process. In such a case, the lower p.d. than 10% is expected in the bridge phase as we have seen in section 3.2. Therefore, the present model predicts that the polarization characteristics in the bridge phase depends on the energy bands. In the pulse and the off-pulse phases, the polarization characteristics do not depend the energy bands very much, because the synchrotron radiation from the secondary pairs takes a main contribution from optical to soft X-ray emissions. Above hard X-ray bands, the inverse Compton process of the secondary pairs will contribute to the emissions. Because the next generation Compton telescope will probably be able to measure the polarization

characteristics in MeV bands, it will be required to model prediction for it, which will be the issue in the subsequent papers.

The authors appreciate fruitful discussion with K.Hirotani, S.Shibata and R.Taam. We thank L.Kuiper for providing COMPTEL, BeppoSax and OSSE data, and the anonymous referee for his/her helpful comments on improvements to the paper. This work was supported by the Theoretical Institute for Advanced Research in Astrophysics (TIARA) operated under Academia Sinica and the National Science Council Excellence Projects program in Taiwan administered through grant number NSC 94-2112-M-007-002, NSC 94-2752-M-007-002-PAE and NSC 95-2752-M-007-006-PAE (J.T. and H.-K. C.), and by a RGC grant number HKU7015/05P (K.S.C.).

REFERENCES

- Blaskiewicz, M., Cordes, J.M. & Wasserman, I. 1991, *ApJ*, 370, 643
- Chen, K., Chang, H.-K. & Ho, C. 1996, *ApJ*, 471, 967
- Cheng, K.S., Ho, C. & Ruderman, M. 1986a, *ApJ*, 300, 500
- Cheng, K.S., Ho, C. & Ruderman, M. 1986b, *ApJ*, 300, 522
- Cheng, K.S., Ruderman, M. & Zhang, L. 2000, *ApJ*, 537, 964 (CRZ00)
- Daugherty, J.K. & Harding, A.K. 1996, *ApJ*, 458, 278
- Dyks, J. & Rudak, B. 2003, *ApJ*, 598, 1201
- Dyks J., Harding A.K. & Rudak B. 2004, *ApJ*, 606, 1125
- Goldreich, P. & Julian, W.H. 1969, *ApJ*, 157, 869
- Hirotani, K. 2006, *Mod. Phys. Lett. A* 21, 1319
- Kanbach, G., Słowikoska, A., Kellner, S. & Steinle, H. 2005, *AIP Conference Proceeding*, 801, 306
- Kirk, J.G., Skjæraasen, O. & Gallant, Y.A. 2002, *A&A*, 388, L29
- Kuiper, L., Hermsen, W., Cusumano, G., Diehl, R., Schönfelder, V., Strong, A., Bennett, K. & McConnell, M. L. 2001, *A&A*, 378, 918

- Muslimov, A.G. & Harding, A.K. 2005, ApJ, 630, 454
- Pétri, J. & Kirk, J.G. 2005, ApJ, 627, L37
- Romani R.W. 1996, ApJ, 470, 469
- Romani, R.W. & Yadigaroglu, I.-A. 1995, ApJ, 438, 314
- Rybicki, G.B. & Lightman, A.P. 1979, Radiative Processes in Astrophysics (New York: Wiley)
- Smith, F.G., Jones, D.H.P., Dick, J.S.B. & Pike, C.D. 1988, MNRAS, 233, 305
- Sollerman, J., Lundqvist, P., Lindler, D., Chevalier, R.A., Fransson, C., Gull, T.R., Pun, C.S.J. & Sonneborn, G. 2000, ApJ, 537, 86
- Takata, J., Shibata, S. & Hirokuni K. 2004, MNRAS, 354, 1120
- Takata, J., Shibata, S., Hirokuni, K. & Chang, H.-K. 2006, MNRAS, 366, 1310
- Thompson, D.J. et al. 1999, ApJ, 16, 297
- Yakovlev, D.G. & Pethick, C.J. 2004, ARA&A, 42, 169
- Zhang, L. & Cheng K.S. 1997, ApJ, 487, 370
- Zhang, L. & Cheng, K.S. 2002, ApJ, 569, 872

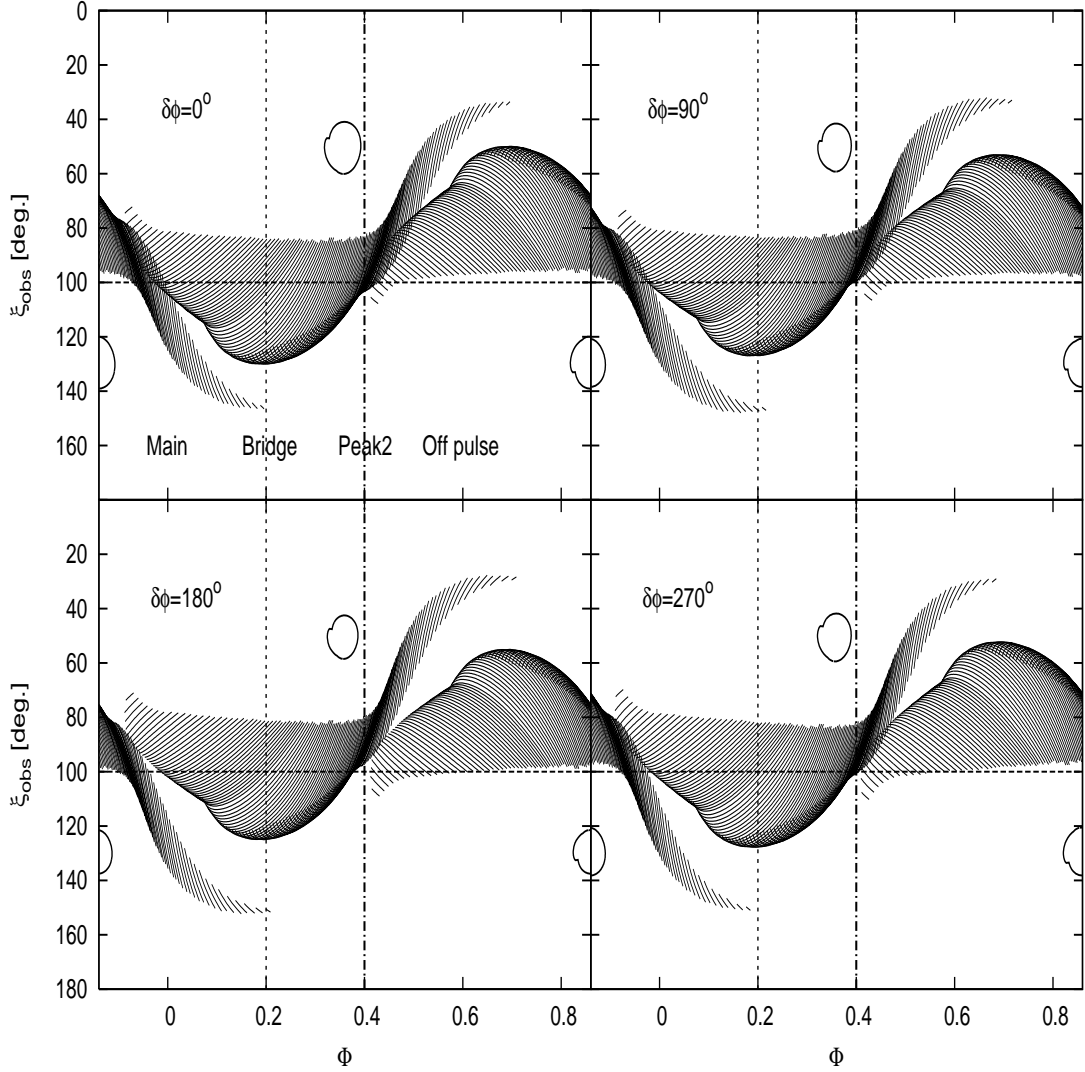


Fig. 1.— Emission projection onto (ξ, Φ) plane for the magnetic surface, $a = 0.94$, of the upper boundary of the outer gap. The inclination angle is $\alpha = 50^\circ$. The emission region extends from $r = 0.67r_n$ to $r = R_{lc}$ or $\rho = 0.9R_{lc}$. Each panel shows the radiations from the positrons with the gyration phase of $\delta\phi = 0^\circ, 90^\circ, 180^\circ$ and 270° , respectively. The thick solid circles in the figure show the shape of the polar cap.

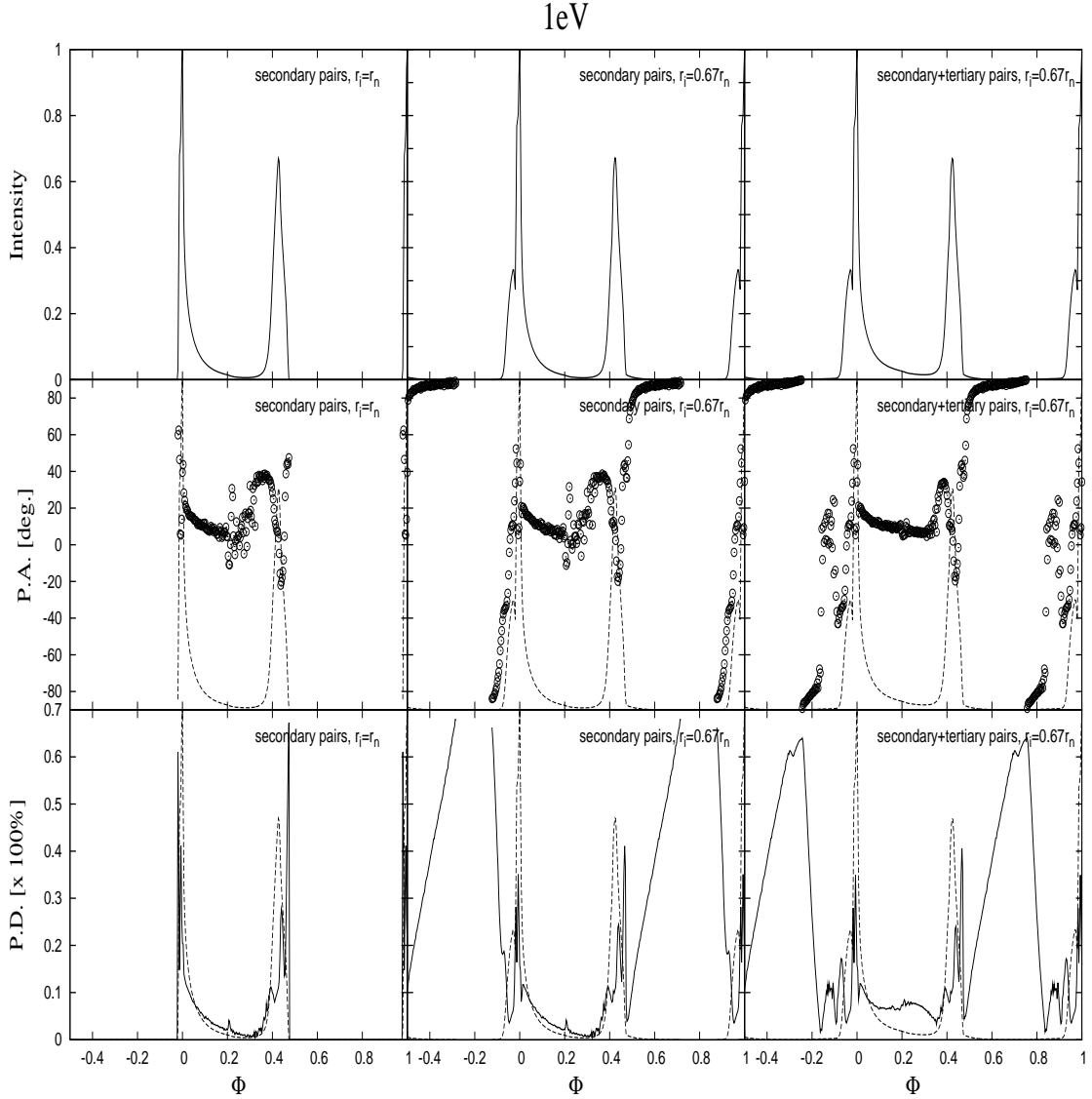


Fig. 2.— Polarization characteristics for three different emission geometries. The left column shows the result for the traditional model, which considers the radiation from the secondary pairs and emission regions extending from the null charge surface, $r_i = r_n$. The middle and right column take into account the radiations from the inside the null charge surface, $r_i = 0.67r_n$, and furthermore the right column considers the effects of the emissions from the tertiary pairs. The upper, middle and lower panels in each column show, respectively, the light curve, the position angle and the polarization degree. The model parameters are $\alpha = 50^\circ$, $\xi = 100^\circ$ and $a = 0.94$.

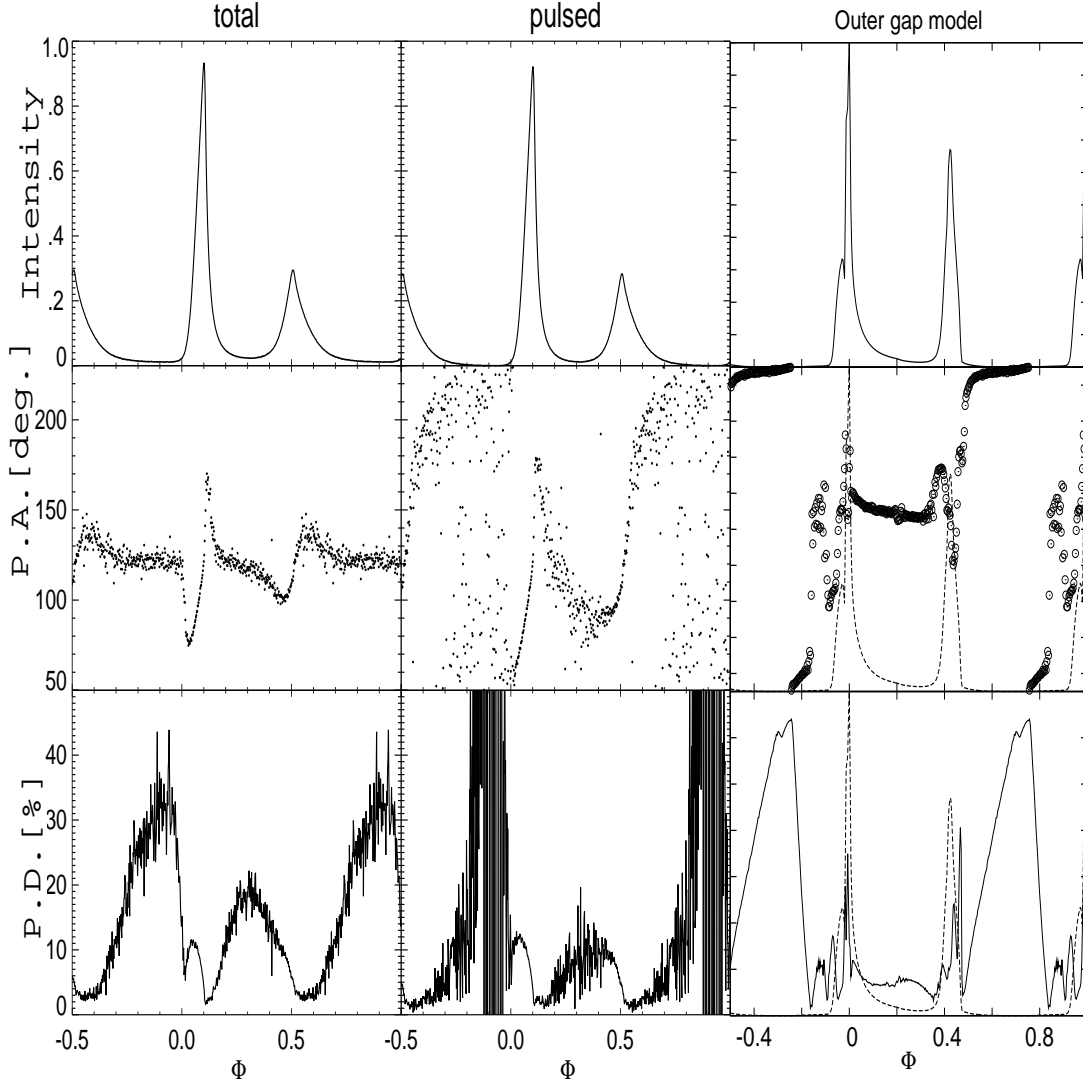


Fig. 3.— Optical polarization for the Crab pulsar. Left: Polarization characteristics for the total emissions from the Crab pulsar. Middle: Polarization characteristics of the emissions after subtraction of the DC level (Kanbach et al. 2005). Right: Predicted polarization characteristics at 1 eV for $\alpha = 50^\circ$, $a = 0.94$, $\xi \sim 100^\circ$ and $r_i = 0.67r_n$. The figures for the Crab optical data was transcribed from DHR04 and was arranged by authors.

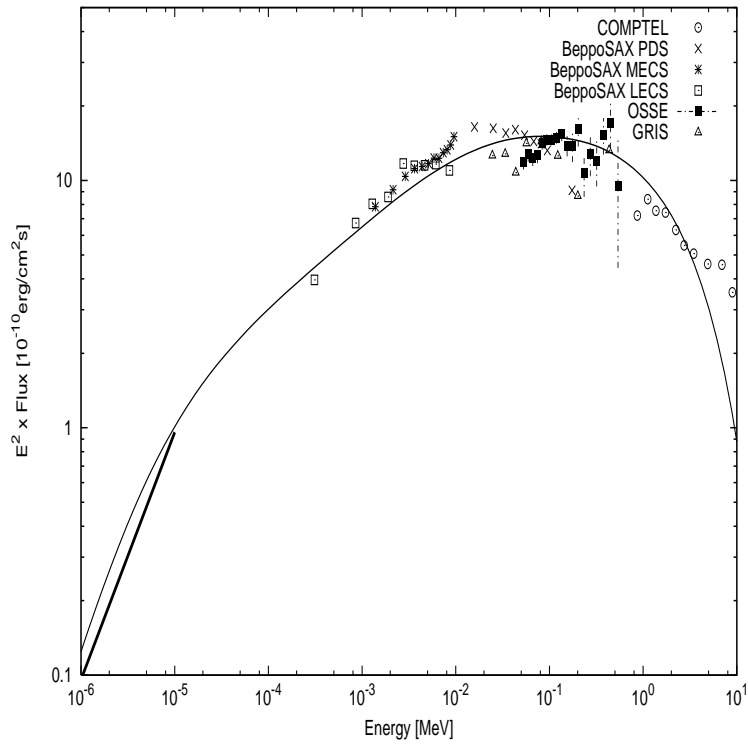


Fig. 4.— The optical-X ray spectrum for the Crab pulsar. Thin solid line shows the expected spectrum for $\alpha = 50^\circ$, $a = 0.94$, $r_i = 0.67$ and $\xi_i \sim 100^\circ$. The X-ray data are taken from Kuiper et al. (2002) and reference therein, and the optical data from Sollerman et al. (2000).

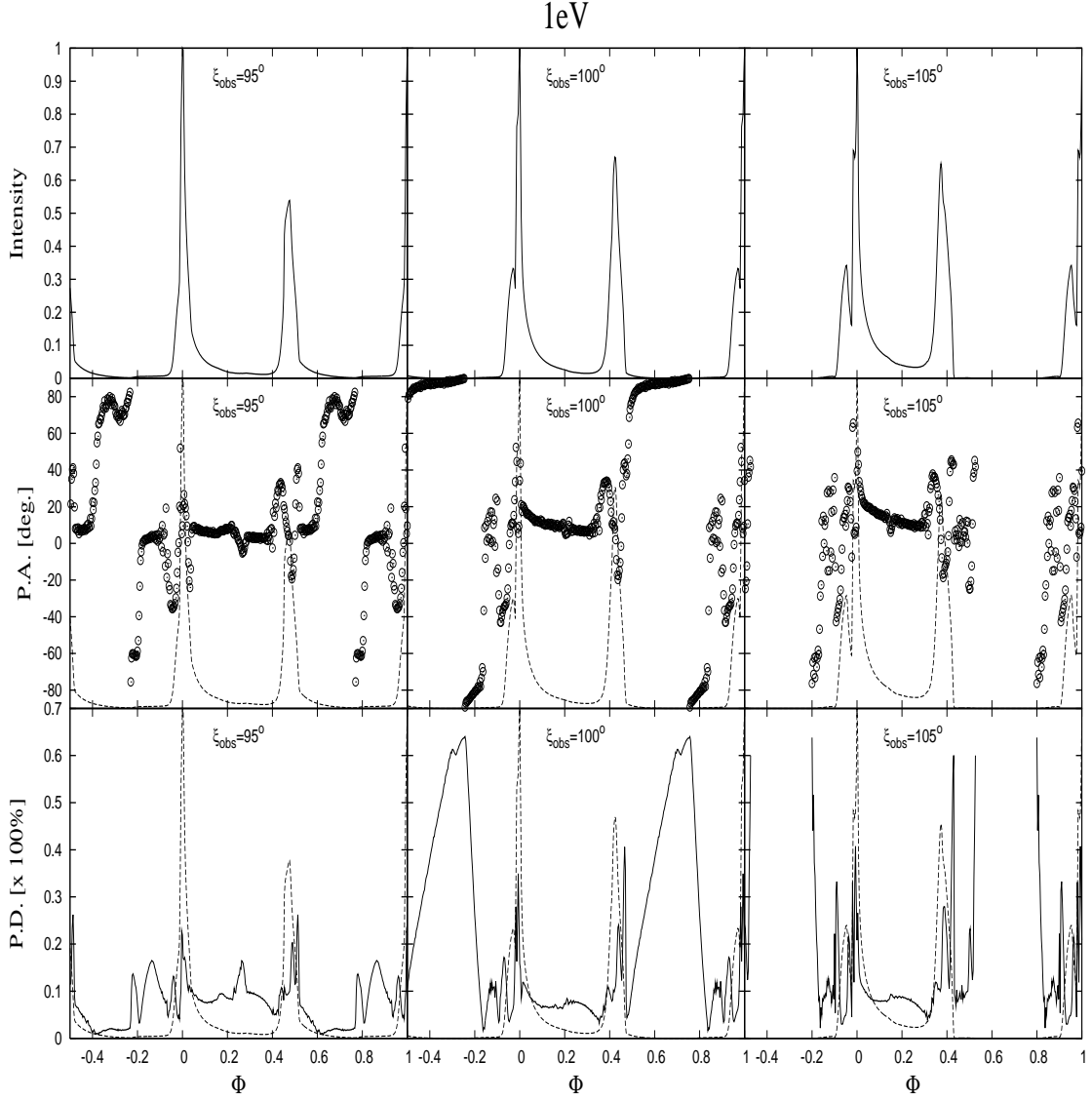


Fig. 5.— The polarization characteristics for three different viewing angles, $\xi \sim 95^\circ$ (left column), 100° (middle column) and 105° (right column), for $\alpha = 50^\circ$, $a = 0.94$ and $r_i = 0.67r_n$.

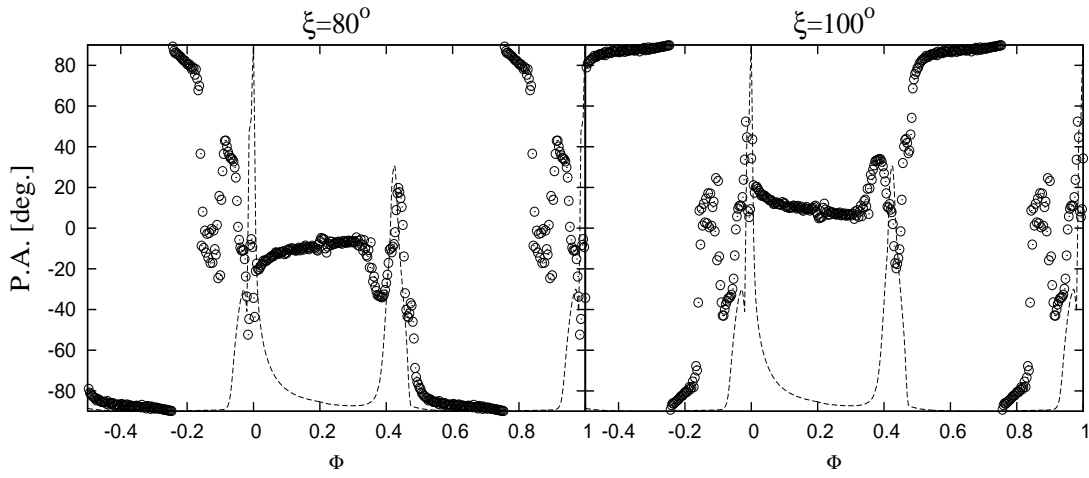


Fig. 6.— The polarization position angle for viewing angles, $\xi \sim 80^\circ$ and 100° , which are mutually symmetric with respect to the rotational equator. The calculations are for $\alpha = 50^\circ$, $a = 0.94$ and $r_i = 0.67r_n$. For the reference, the light curve are overplotted.

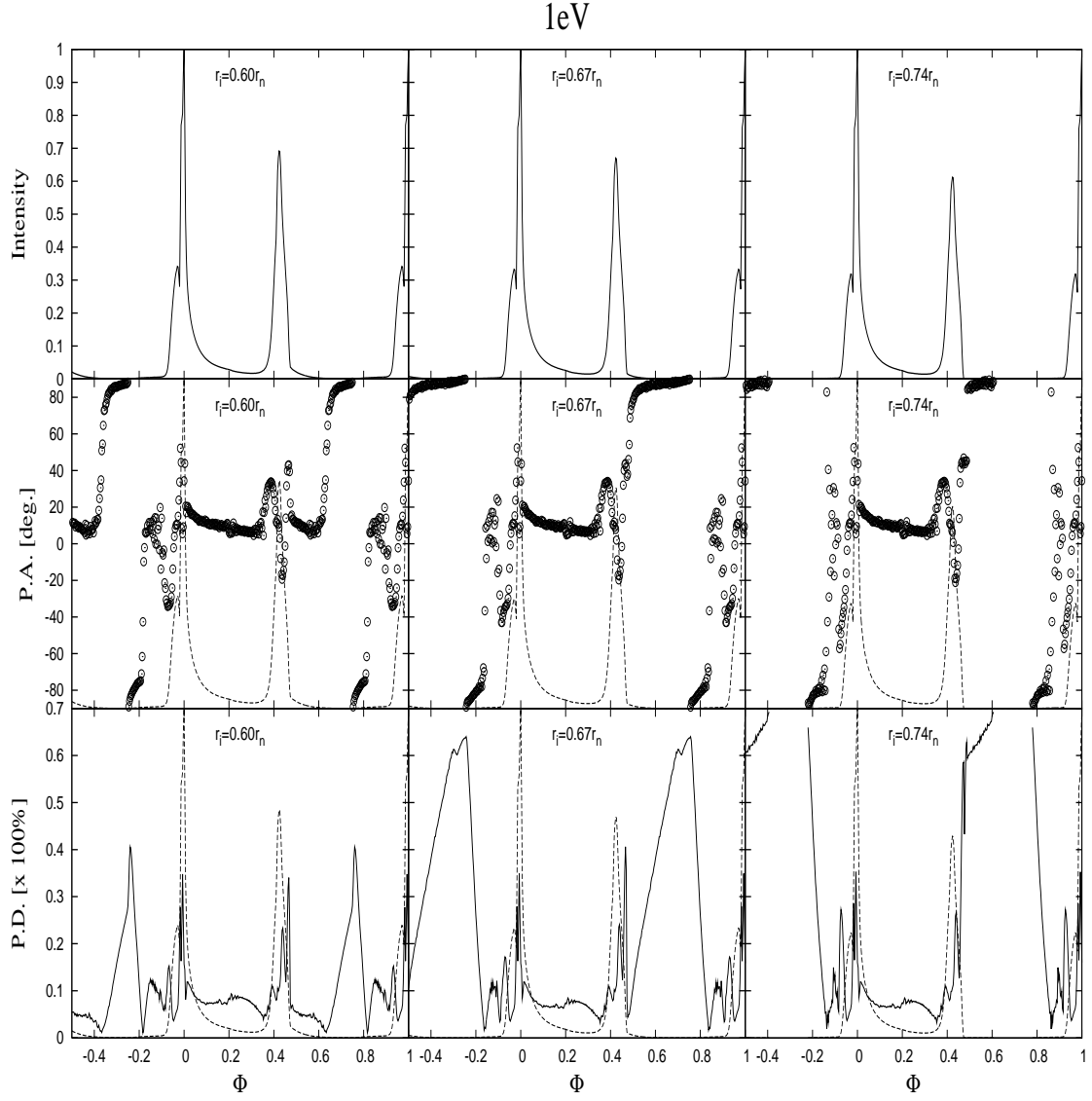


Fig. 7.— The polarization characteristics for three different positions of the inner boundary, $r_i = 0.60r_n$ (left column), $0.67r_n$ (middle column) and $0.74r_n$ (right column), for $\alpha = 50^\circ$, $a = 0.94$ and $\xi \sim 100^\circ$.

		$a = \theta_u/\theta_{lc}$						
		0.9	0.91	0.92	0.93	0.94	0.95	0.96
α	40°	*	$\xi \sim 100^\circ$ $r_i \sim 0.75$	102.5° 0.65	105° 0.58	107.5° 0.50	110° 0.43	112.5° 0.37
	50°	*	*	*	$\xi \sim 97^\circ$ $r_i \sim 0.78$	100° 0.67	105° 0.46	107.5° 0.37
	60°	*	*	*	*	*	$\xi \sim 100^\circ$ $r_i \sim 0.53$	105° 0.30

Table 1: Expected viewing angle and the position of the inner boundary for various inclination angle α and the fraction angle of the gap upper surface $a = \theta_u/\theta_{cl}$, where θ_u is the polar angle of the footpoint of the magnetic surface of the gap upper boundary and θ_{cl} is that of the magnetic surface tangent to the light cylinder for the rotating dipole field. For each α and a , the viewing angle ξ is chosen to explain the phase separation of the two peaks, and the position of the inner boundary r_i is determined so that the p.a. has large swings at the both peaks and the p.d. in the off-pulse phase becomes about $\sim 60\%$.

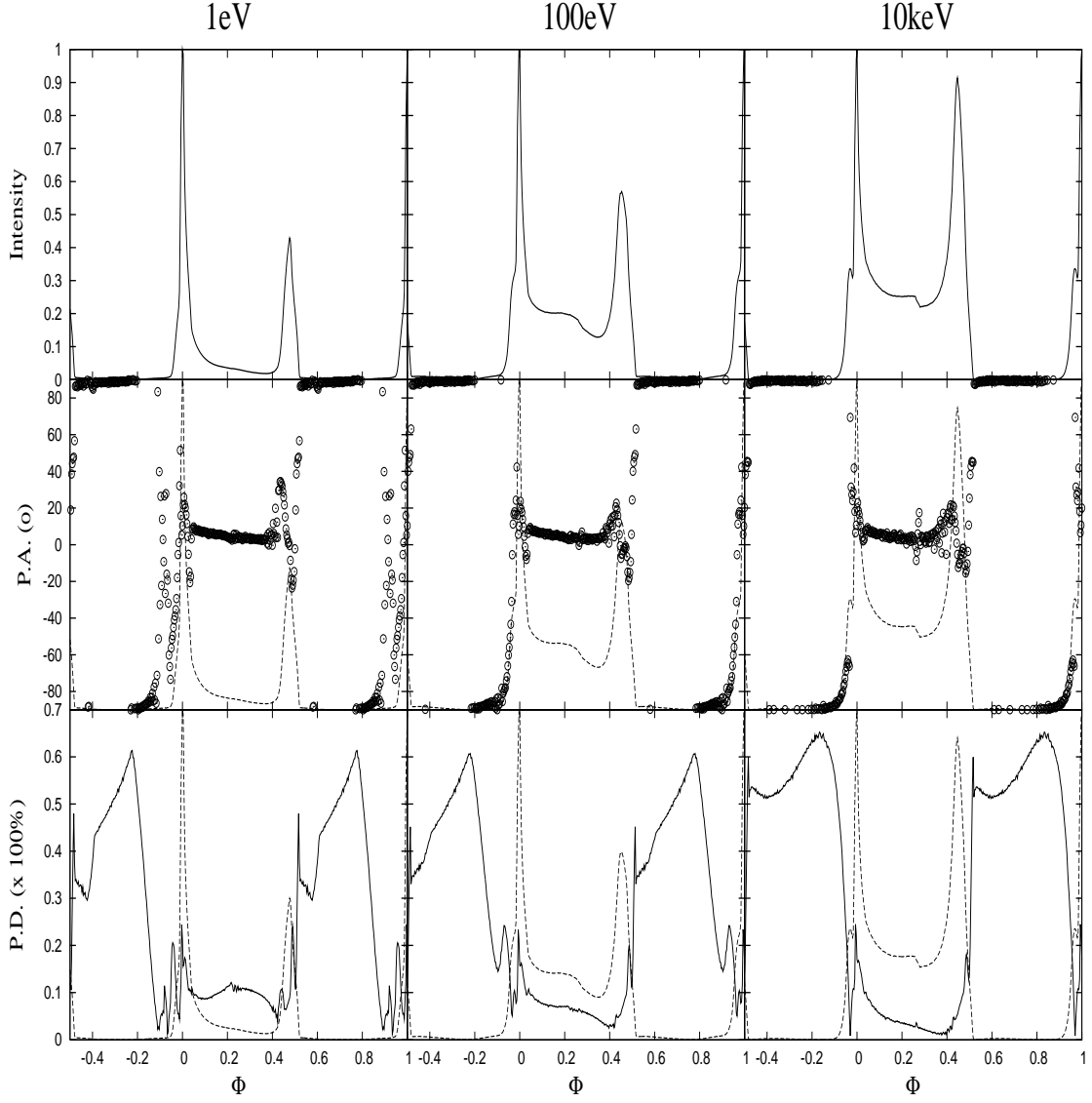


Fig. 8.— The polarization characteristics of three energy bands, 1 eV (left column), 100 eV (middle column) and 10 keV (right column) for $\xi \sim 95^\circ$, $\alpha = 50^\circ$, $a = 0.94$ and $r_i = 0.85r_n$. The present model predicts the energy dependent polarization characteristics.